Comparison of formation and evolution of radiation-induced defects in pure Ni and Ni–Co–Fe medium-entropy alloy

Lin Lang(稂林)[1], Huiqiu Deng(邓辉球)[2,†], Jiayou Tao(陶家友)[1], Tengfei Yang(杨腾飞)[3], Yeping Lin(林也平)[3], and Wangyu Hu(胡望宇)[3]

[1] *Key Laboratory of Hunan Province on Information Photonics and Freespace Optical Communications, School of Physics and Electrical Sciences, Hunan Institute of Science and Technology, Yueyang* 414006, *China*
[2] *School of Physics and Electronics, Hunan University, Changsha* 410082, *China*
[3] *College of Materials Science and Engineering, Hunan University, Changsha* 410082, *China*

(Received 14 June 2022; revised manuscript received 8 August 2022; accepted manuscript online 12 August 2022)

High-entropy alloys (HEAs) and medium-entropy alloys (MEAs) have attracted a great deal of attention for developing nuclear materials because of their excellent irradiation tolerance. Herein, formation and evolution of radiation-induced defects in NiCoFe MEA and pure Ni are investigated and compared using molecular dynamics simulation. It is observed that the defect recombination rate of ternary NiCoFe MEA is higher than that of pure Ni, which is mainly because, in the process of cascade collision, the energy dissipated through atom displacement decreases with increasing the chemical disorder. Consequently, the heat peak phase lasts longer, and the recombination time of the radiation defects (interstitial atoms and vacancies) is likewise longer, with fewer deleterious defects. Moreover, by studying the formation and evolution of dislocation loops in Ni–Co–Fe alloys and Ni, it is found that the stacking fault energy in Ni–Co–Fe decreases as the elemental composition increases, facilitating the formation of ideal stacking fault tetrahedron structures. Hence, these findings shed new light on studying the formation and evolution of radiation-induced defects in MEAs.

Keywords: medium-entropy alloy, molecular dynamics simulations, radiation-induced defects, stacking fault energy

PACS: 61.72.–y, 61.80.–x, 61.82.–d, 71.15.Pd **DOI:** 10.1088/1674-1056/ac891e

1. Introduction

The development of metal alloys is arguably one of the oldest sciences, and it has a history of more than 3000 years. Most research and applications focus on alloys with a principal element, such as aluminium alloy and iron steel systems.[1] Recently, the accelerated development of new technologies for efficient energy production demands new materials that can tolerate extreme environments and operate reliably at high temperatures. To meet the demand, medium-entropy alloys (MEAs) in ternary systems and high-entropy alloys in quaternary or quinary systems (HEAs) have been widely investigated,[2–9] and have received tremendous attention. At least part of this interest stems from the fact that some exhibit intriguing and exceptional mechanical properties that are of challenge to interpret. For example, MEAs exhibit extraordinary properties compared with traditional alloys, such as high thermal stability and hardness,[10,11] toughness,[8] high-temperature strength,[12,13] great wear,[14] fatigue resistance,[15,16] and excellent corrosion resistance,[5,8,17,18] which are attributed to the complicated random arrangement of the alloying elements and local chemical environment at the atomic level.

Theoretical and experimental studies reveal that MEAs have higher radiation tolerance[2,19–22] than the corresponding pure elements. Due to the complex composition and a high degree of lattice distortion, MEAs can tailor the energy dissipation process and the recovery rate of radiation damage in the early stage of the displacement cascade. The previous studies[23,24] clearly demonstrates that modifying alloy compositional complexity will enable to control defect dynamics at the early stage of radiation damage and to ultimately enhance radiation tolerance at the later stage under extreme radiation conditions. On the other hand, structural complexity is also an important aspect to design radiation tolerant material. Zhang *et al.*[19] reported that lattice distortions and compositional complexities in MEAs can effectively reduce the mean free path, conductivity and thermal conductivity of electrons, thus greatly delaying the evolution of defects caused by ion radiation at room temperature. Furthermore, formation energies, migration barriers and diffusion pathways of radiation defects can also be tailored by the lattice distortions and compositional complexities, thereby modifying defects generation and interstitial–vacancy recombination in the early stages of radiation. For Ni-based MEA systems, from pure Ni to more complexes five-element HEAs, as the chemical disorder increases, the energy dissipation reduces, resulting in fewer defects, thereby inhibiting the accumulation of radiation damage defects.[19]

Radiation damage depends on the formation and evolution of radiation-induced defects, including the evolution of

[†]Corresponding author. E-mail: hqdeng@hnu.edu.cn

© 2022 Chinese Physical Society and IOP Publishing Ltd

the displacement cascade and migration as well as accumulation of survival defects. The evolution of the displacement cascade is the primary radiation damage process and is an atomic level phenomenon. Additionally, the cascade collision process lasts only for a few nanoseconds, so the formation and evolution of defects cannot be observed through experiments. Therefore, molecular dynamics (MD) simulations provide a useful tool for a detailed understanding of the underlying mechanisms at atomistic scales. A recently published study indicates that MEAs are more resistant to radiation damage than the corresponding pure elements.[25–29] For example, in our previous study,[28] binary Ni-based alloys had higher defect recombination rates than pure Ni, especially Ni–Fe alloy. Although some efforts have been made to investigate HEAs or MEAs in experiments and MD simulations, their fundamental radiation damage properties, including details related to defect production and dislocation loop evolution processes in these new materials, remain unclear. Therefore, in this article the damage defect evolution and dislocation loop formation of ternary NiCoFe MEAs under different primary knock-on atom (PKA) energies are investigated, and the results are compared with those of pure Ni.

2. Simulation method

In this work, MD simulations were performed using the large-scale atomic/molecular massively parallel simulator (LAMMPS)[30] to study the defect behavior in pure Ni and NiCoFe MEA under different PKA energies. The modified embedded-atom method potential[31] developed by Choi *et al.*[32] was chosen to describe the interatomic interactions, which have well reproduced the defect properties.[33,34] To simulate the interatomic interactions in a minute range, the repulsive part of the pair potentials was connected smoothly to the Biersack–Zeigler universal function.[35] The displacement cascade simulation boxes were $60a \times 60a \times 60a$ containing 864000 atoms for 10 keV, $80a \times 80a \times 80a$ containing 2048000 atoms for 30 keV, and $120a \times 120a \times 120a$ containing 6912000 atoms for 50 keV, respectively. The NiCoFe HEA simulation cell was constructed by creating a random mixture of elements in a well-defined face-centered cubic (FCC) crystal, which contained Ni, Co, and Fe elements in an equimolar ratio. According to the present interatomic potential, the equilibrium lattice parameter (a) of 3.52 Å was used for pure Ni, which is close to the experimental value ($\sim$ 3.52 Å for Ni[19]). For the NiCoFe HEA, the initial a was determined to be the minimum energy position in the plot showing the total energies versus the various lattice constants of a crystal under investigation, where the internal energies of the crystal for different lattice constants were calculated with energy minimization. Since a slightly varies with the randomly distributed NiCoFe HEAs, it is determined to be 3.569 Å by averaging over 10 NiCoFe HEAs with randomly mixed elements in an FCC crystal, which is close to the value obtained in Ref. [36]. The collision cascades were initiated by giving a Ni atom with the PKA energy from 10 keV to 50 keV within the constant NVE ensemble, and the $\langle 135 \rangle$ direction was chosen as the PKA direction to avoid the channeling effect. A variable MD time step (0.001 fs to 1.0 fs) was employed to speed up the simulations, which depends on the maximum displacement (each atom did not move more than 0.02 Å per time step) in the system. To obtain the representative statistics, 20 cascade simulations were repeated for each set of cascade energy. Each cascade simulation was run for 150 ps, which is sufficient to allow the cascade to anneal and return to thermal equilibrium. A thermostat was applied at the sides of the box by rescaling the velocities of the atoms in a 5-Å layer width around the simulation boxes, which can extract the excess kinetic energy arising from the cascade and minimize the interaction of heat wave with periodic images of itself.

To analyze the evolution of surviving defects from the displacement cascade, a Wigner–Seitz (W–S) defect analysis was employed to detect point defects and defect clusters. The clustering of defects was calculated with a relatively strict connectivity cutoff limited to the first-nearest neighbor. A dislocation extraction algorithm (DXA)[37] in the open-source application OVITO[38] was also used to visualize the dislocation loops in defect clusters and to distinguish the shape of the defect cluster in the same crystal structure.

3. Results

3.1. Defect generation and illustration

Neutron radiation causes many defects in materials, such as point defects, dislocation loops and voids, which affect the performance of materials. Figure 1 shows the illustration of defects in Ni and NiCoFe MEAs at different stages during the cascade process at $E_{\mathrm{PKA}} = 30$ keV. Figures 1(a) and 1(b) show the corresponding illustration of defects in the thermal peak stage ($\sim$ 1 ps). Figures 1(c) and 1(d) present the residual defects in the systems (150-ps). The number of defects in Ni is far less than that in NiCoFe MEAs at the thermal peak stage (Figs. 1(a) and 1(b)). However, there are considerable residual defects at the quenched stage in Ni than that in NiCoFe MEAs, implying that NiCoFe MEAs have more defects than pure Ni at the thermal peak stage. However, after the recombination of defects, there were fewer residual defects. Hence, the recombination rate of defects in ternary NiCoFe MEAs is higher than that of pure Ni.

To explain the difference in the number of displacement atoms in the thermal peak stage between Ni and NiCoFe MEAs, the threshold displacement energy (E_{d}) of atoms along specific directions was calculated (Table 1). In the simulation,

an atom at the center of the cell was given with kinetic energy along a specific crystallographic direction. The threshold displacement energy, which is defined as the minimum amount of transferred kinetic energy necessary to permanently displace an atom from its original lattice site to form a stable defect, is a key parameter on determining the atomic displacement rate under irradiations. Table 1 shows that the threshold displacement energy in NiCoFe MEAs is less than that of pure Ni. Furthermore, the E_d values calculated along the different directions are different, showing a strong directional dependence, which is consistent with the results of many previous studies. The lowest threshold displacement energy for Ni and NiCoFe MEAs occurs in the [135] direction. A replacement collision sequence in this direction may make it easier for lattice atoms to leave the lattice position and to reach other positions, forming interstitial atoms or other damage defects. The calculation results of Cu in previous studies[39,40] also show that E_d in the close-packed direction is higher than those in other directions. Moreover, the threshold displacement energy of Ni along the four directions is higher than that in NiCoFe MEAs, so there are fewer displacement atoms formed during the thermal peak stage.

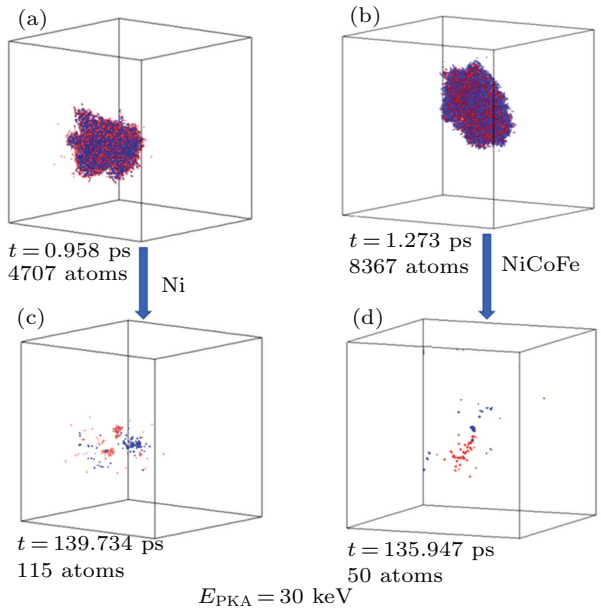


Fig. 1. The illustration of defects in the thermal peak stage and the end of the cascade simulation for pure Ni [(a), (c)] and NiCoFe MEAs [(b), (d)]. Red and blue represent interstitials and vacancies, respectively.

Table 1. Threshold displacement energy in different PKA directions. For the NiCoFe MEAs, each result is an average of 10 different random samples with different configurations.

	Threshold displacement energy E_d (eV)			
System	⟨100⟩	⟨110⟩	⟨111⟩	⟨135⟩
Ni	35	45	54	32
Ni–Co–Fe	26(±12)	28(±14)	45(±17)	25(±8)

Figure 2 shows the variation of the residual Frenkel pairs with different PKA energies, which reveals that the average number of residual Frenkel pairs increases as the PKA energy increases. This trend occurs because higher recoil energy can induce much more vacancies and interstitials. Moreover, it was found that the average number of residual Frenkel pairs, showing a strong dependence on the elemental composition, and the number of residual Frenkel pairs in pure Ni are greater than those in NiCoFe MEAs. The NiCoFe MEAs have more defects than Ni (Fig. 1) in the thermal peak stage, whereas there are few residual defects in NiCoFe MEAs after the recombination of defects. The defect recombination rates of Ni and NiCo, NiFe, NiCoFe MEAs were compared, and the results are listed in Table 2. The calculation formula is

$$\eta = \frac{N_d - N_{FP}}{N_d} \times 100\%,$$

where N_d is the number of FPs in the peak damage state, and N_{FP} is the number of surviving defects. The results for NiCo and NiFe are taken from Ref. [28], which are also confirmed by experiments.[19,27] Thus, from pure Ni to more complex ternary MEAs, the self-recombination ability of defects is enhanced, that is, the radiation resistance is enhanced.

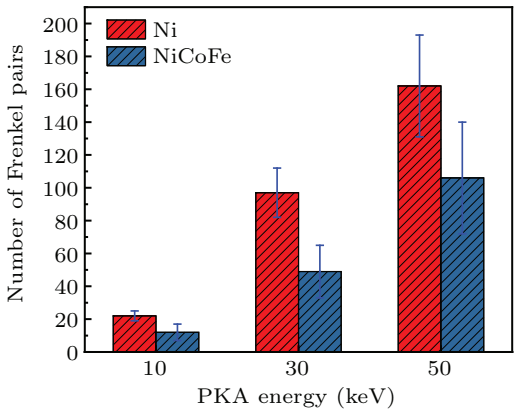


Fig. 2. The average number of surviving Frenkel pairs for pure Ni and NiCoFe MEAs, averaged from 20 cascade simulations with 10 keV, 30 keV and 50 keV energies at 300 K. The error bar comes from the statistical average of 20 results.

Table 2. The recombination rate of defects (η) in pure Ni and NiCo, NiFe, NiCoFe MEAs.

Alloys	η (%)
Ni	96.6
NiCo	98.2
NiFe	98.9
NiCoFe	99.0

Figure 3 show the defect quantitative analysis. At the same PKA energy, the average number of vacancy and interstitial clusters in Ni is always more than those in NiCoFe MEAs, and the cluster size of most vacancy and interstitial clusters is 3–20 atoms. Also, there are no large vacancy (> 20 atoms) and interstitial (> 50 atoms) clusters in NiCoFe MEAs at E_{PKA} = 30 keV (Fig. 3(a)), and even none of the large vacancy and interstitial clusters (> 50 atoms) were found at $E_{PKA} = 50$ keV (Fig. 3(b)). Compared with Figs. 3(a) and 3(b), the number

of vacancies and interstitial clusters increases as the PKA energy increases, and it is difficult to form large-size vacancies (voids) and interstitial clusters in NiCoFe MEAs compared to pure Ni, the same conclusion can be found in binary Ni–Co and Ni–Fe binary Ni-based alloys.[28] Furthermore, it was observed that most of the large interstitial clusters of NiCoFe MEAs were immobile and remained in the defect production region, whereas the interstitial clusters were movable in Ni. Also, most vacancies in NiCoFe MEAs are likely annihilated by interstitials in the cascade formation range. Thus, the size of the vacancies and interstitial clusters in NiCoFe MEAs is smaller than that of pure Ni. This result agrees with those of Lu *et al.*[3] and Tsai *et al.*[41]

To explain the higher defect recombination rate in ternary NiCoFe MEAs, the potential energy evolution of Ni and Ni–Co–Fe system during the cascade (Fig. 4) was studied, and the pair distribution function $g(r)$ of the interstitials and vacancies of Ni and NiCoFe MEAs at the thermal peak stage is illustrated (Fig. 5). The results shown in Figs. 4(a)–4(c) indicate that as the PKA energy increases, the potential energy takes a long time to attain equilibrium. For example, in Figs. 4(a)–4(c), the time for the potential energy of Ni to reach equilibrium is $\sim$ 30, 50, and 70 ps for 10, 30, and 50 keV, respectively. Moreover, at the same PKA energy, the potential energy of NiCoFe MEAs takes a longer time than Ni to attain equilibrium. Zhang *et al.*[42] has pointed out that the inefficient heat conduction results in more localized heat, and slow dissipation of radiation energy leads to enhanced defect recombination. Therefore, this trend in Figs. 4(a)–4(c) indicates that NiCoFe MEAs have slower energy dissipation than Ni in the cascade, which means that in NiCoFe MEAs, the defects generated at the peak stage take a longer time to recombine to reach equilibrium. Zhang *et al.*[19] also obtained the similar results. Through experiments, they found that with increasing chemical disorder from pure Ni to binary and more complex HEAs, the chemical disorder could lead to a substantial reduction in the electron mean free path and decrement orders of magnitude in the electrical and thermal conductivity. The subsequently slow energy dissipation affects defect dynamics at the early stages and consequentially may result in less deleterious defects.

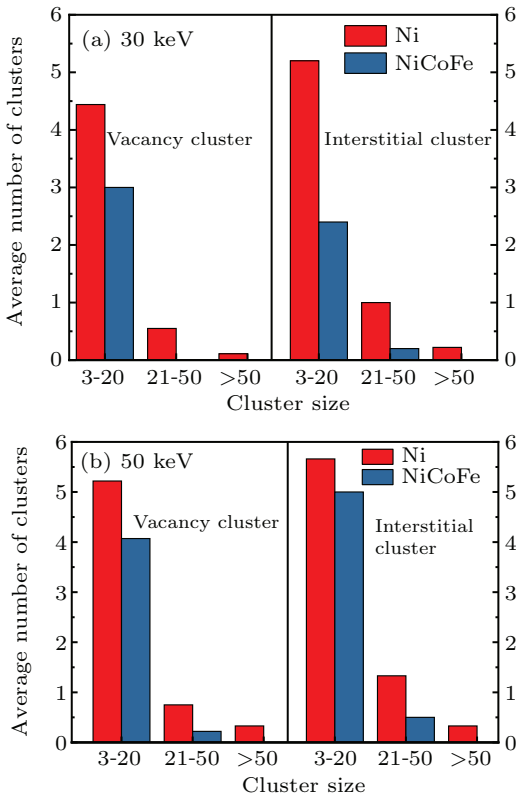


Fig. 3. Point defect cluster size distributions in Ni (red) and NiCoFe (blue) for simulation energies of 30 keV (a) and 50 keV (b) at 300 K (due to the low number of defects at 10 keV, it is not shown).

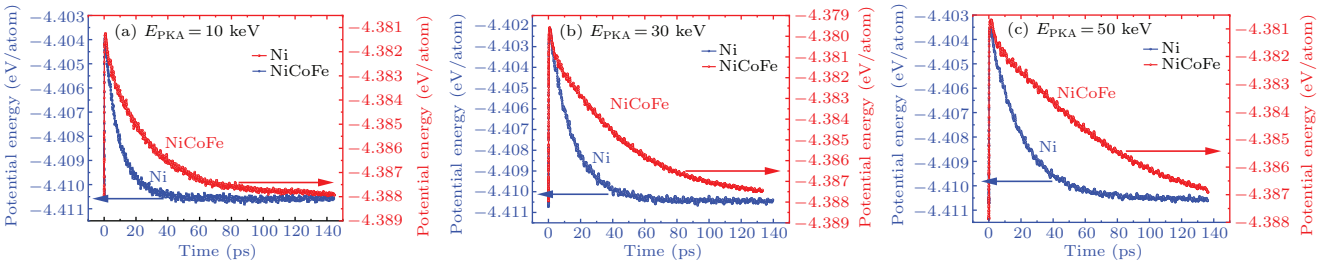


Fig. 4. Evolution of average potential energy of Ni and NiCoFe MEAs during a cascade: (a) $E_{PKA} = 10$ keV, (b) $E_{PKA} = 30$ keV, and (c) $E_{PKA} = 50$ keV.

In statistical mechanics, the radial distribution function (or pair correlation function) $g(r)$ in a system of particles (atoms, molecules, colloids, etc.) can describe how the density varies as a function of distance from a reference particle. According to the definition of $g(r)$ and the existing results,[43] it is realized that $g(r)$ function can effectively describe the distribution of different particles in the system. Therefore, we use the $g(r)$ function to describe the distribution (aggregation or dispersion) of vacancies and interstitial defects after irradiation. Figure 5 shows that the position of the first peaks on the $g(r)$ curves of Ni and NiCoFe MEAs do not align, stabilized at 2.47 Å and 2.53 Å for NiCoFe MEAs and Ni, respectively. Also, the height of the first peak in NiCoFe MEAs is higher than that in Ni, indicating the distance between interstitial and vacancy atoms in NiCoFe MEAs being smaller than that in Ni, and tending to be more agglomeration. The agglomeration

increases the self-combination probability of vacancy and interstitial atoms, that is, the closer the distance between the vacancy and interstitial atoms, the more noticeable the agglomeration, and the higher the recombination rate of the defects.

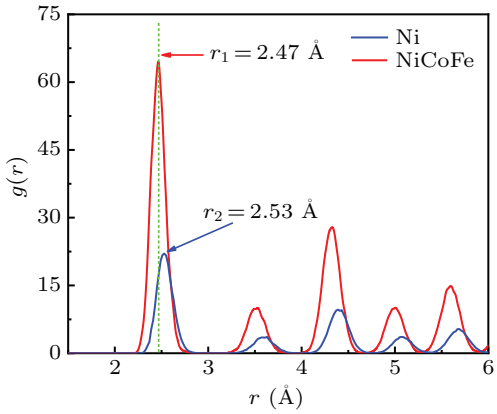


Fig. 5. The pair distribution function ($g(r)$) of interstitial and vacancy atoms in the thermal peak stage of Ni (black line) and NiCoFe MEAs (red line). The vertical dot lines are for guiding the eyes.

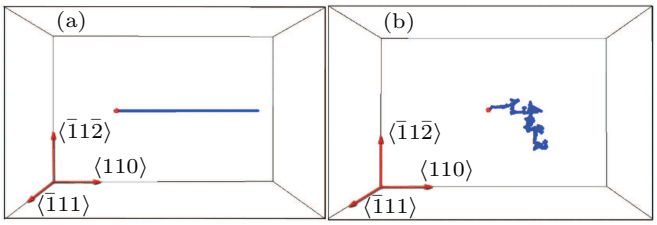


Fig. 6. Trajectories of the center of a nine-interstitial cluster (a) in Ni at 800 K and (b) in NiCoFe MEAs at 1200 K.

Furthermore, the migration of nine interstitial clusters in bulk Ni and NiCoFe MEAs were studied. Figure 6 presents migration trajectories of the mass centers for nine interstitial clusters in pure Ni and NiCoFe MEAs. In pure Ni, the mass center of the interstitial clusters moves in a one-dimensional (1D) model along the ⟨110⟩ direction. However, for NiCoFe MEAs, the mass center of interstitial clusters randomly changes directions, thus forming several 1D ⟨110⟩ segments. The shorter 1D migration segment and more frequent directional changes of interstitial clusters in NiCoFe MEAs will eventually lead to a dominant 3D migration behavior, which is similar to the migration of Ni–Co and Ni–Fe in the literature.[3,44] Previous experiments[3,45,46] and computational studies[47,48] reported that small clusters of self-interstitial atoms can migrate one-dimensionally along the close-packed directions of atoms in the lattice. In simple metals, such as Cu and Ni, the migration barrier of small interstitial clusters is low for 1D motion. Therefore, they can migrate quickly and along the direction of the Burgers vector. This 1D motion may cause the interstitial atoms to migrate farther without recombining with the local area's vacancy, thus, being in high-vacancy supersaturation behind and leading to significant void swelling. Thus, for pure Ni, the interstitial cluster migrates along the ⟨110⟩ direction with 1D motion. The interstitial cluster can migrate a long distance without encountering numerous vacancies, leaving a high-vacancy supersaturation behind to be susceptible to the detrimental void formation (large vacancy clusters). The difference is that in NiCoFe MEAs, the interstitial clusters move in a 3D motion, and there are more opportunities to be annihilated by the vacancy in the cascade formation region, resulting in a higher defect recombination rate. Lu *et al.*[3] reported the similar results in the Ni–Fe system through experiments. The difference in the manner of migration of interstitial clusters between Ni and NiCoFe MEAs may account for the higher defect recombination rate of NiCoFe MEAs than that of Ni.

3.2. Dislocation loop evolution

Once the size of defect clusters gathers to a certain extent, they may form a dislocation loop, lead to embrittlement and swelling, and deteriorate the structural and mechanical properties of the alloy. Figure 7 shows the distribution of dislocation loops/networks formed in Ni and NiCoFe MEAs under 50 keV PKA energy. The dislocation loops/networks formed by radiation are mainly Shockley, Frank, stair-rod and perfect dislocation loop/networks. The stair-rod dislocation network is mainly formed by vacancy clusters, so it is a vacancy dislocation network, and it often forms a stacking fault tetrahedra (SFT) structure (Fig. 7(b)). Interestingly, only the Frank loop exists in Ni and NiCoFe MEAs as a complete circle, which is analogous to the results of Levo *et al.*[49] To quantitatively describe the dislocation loop generated after radiation, the average length values of the dislocation loop formed in the 20 calculation results were calculated, as listed in Table 3.

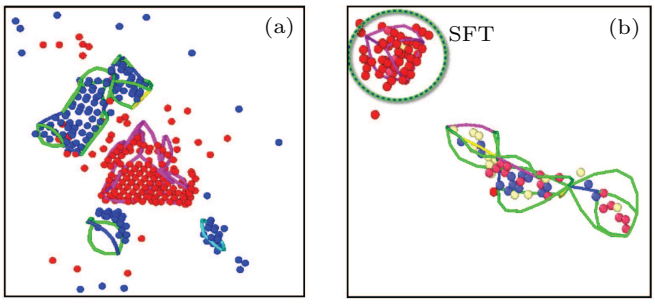


Fig. 7. Snapshot of the dislocation networks and defect clusters in Ni (a) and NiCoFe MEAs (b), at the $E_{\mathrm{PKA}} = 50$ keV. The lines of different colors represent dislocations with different Burgers vectors, where green is a Shockley (1/6⟨112⟩), purple a stair-rod (1/6⟨110⟩), light blue a Frank (1/3⟨111⟩), yellow a Hirth (1/3⟨001⟩) and dark blue a perfect dislocation (1/2⟨110⟩). The red balls represent vacancies, other balls represent interstitials, the blue balls are Ni interstitials, the light red balls are Co interstitials, and yellow balls are Fe interstitials.

In Table 3, the average length of the dislocation loop is denoted by an index *N*–*L*, where *N* is the average number of segments of the dislocation loop and *L* represents the average length of the dislocation loops. Table 3 shows that the average

number and length of the dislocation loops increase accordingly as the PKA energy increases, and the average number of segments and length of the dislocation loops in Ni are greater than those in NiCoFe MEAs under the same PKA energy. In addition, the presence of dislocation loops was only found in Ni at 10 keV. In contrast, the main dislocation loops are of the $1/6\langle 112\rangle$ and $1/6\langle 110\rangle$ dislocation loops, whereas the $1/2\langle 110\rangle$ and $1/3\langle 111\rangle$ dislocation loops are almost rare. Also, most interstitial-type dislocation loops exist in the form of complex dislocation nets, unlike the complete loops in W bulk.[50]

Unlike the BCC structure, there are various types of dislocation reactions in the FCC crystal. To investigate the dislocation reactions in FCC crystals, different types of complete dislocation loops in Ni and Ni–Co–Fe MEAs were constructed, and detailed information on the construction of dislocation loops can be found in the literature.[51] A complete $1/2\langle 110\rangle$ dislocation loop was constructed in Ni and Ni–Co–Fe bulks, and its evolution is shown in Fig. 8.

Figures 8(a) and 8(b) show that in Ni and NiCoFe MEAs, the $1/2\langle 110\rangle$ complete dislocation loop undergoes the energy minimization relaxation, and the dislocation reaction is dissociated into two $1/6\langle 112\rangle$ dislocation lines by the dislocation reaction. The reason is that in FCC metals, the slip of crystal occurs between close-packed $\{111\}$ atomic planes and the observed slip direction is $\langle 110\rangle$. For a better understanding, the slip planes ($\{111\}$) of the FCC structure are drawn, as shown in Fig. 8(c). One layer is represented by the full circles, *A*, the second identical layer rests at the sites marked as *B* and the third takes the position *C*. Consider the movement of the layers when they are sheared over each other to produce a displacement in the slip direction. The *B* layer of atoms, instead of moving from one *B* site to the next *B* site over the top of the *A* atoms (vector b_1), will move first to the nearby *C* site along the 'valley' between the two *A* atoms (vector b_2), and then to the new *B* site via the second valley (vector b_3). Thus, the *B* plane will slide over the *A* plane in a zig-zag motion.

As shown for the $\{111\}$ plane in Fig. 8(d), the perfect dislocation with Burgers vector $b_1 = 1/2\langle 110\rangle$ will be energetically more favorable for the *B* atoms to move to *B* site via *C* site. This situation implies that the dislocation glides as two partial dislocations ($1/6\langle 112\rangle$), one immediately after the other. The first and second partial dislocations have Burgers' vectors b_2 and b_3, respectively, each with the form of $1/6\langle 112\rangle$. The perfect dislocation with Burgers vector b_1, therefore, splits up or dissociates into two dislocations b_2 and b_3, according to the reaction

$$\frac{1}{2}[\bar{1}10] \rightarrow \frac{1}{6}[\bar{2}11] + \frac{1}{6}[\bar{1}2\bar{1}]. \tag{1}$$

Also, depending on Frank's rule, the splitting reaction (Eq. (1)) is energetically favorable, for $b_1^2 = \frac{1}{2}a^2$, which is $> b_2^2 + b_3^2 = \frac{1}{3}a^2$. Thus, the results obtained here demonstrate that the $1/2\langle 110\rangle$ dislocation loop is dissociated and is consistent with the dislocation theory. The mixed dislocation network of $1/6\langle 112\rangle$ formed after radiation may be constituted by decomposing the portion of the $1/2\langle 110\rangle$ dislocation loop.

Table 3. Statistically of the average length of the dislocation loop formed in the 20 results.

E_{PKA}	System	Dislocation type (length (Å))			
		$1/6\langle 110\rangle$	$1/6\langle 112\rangle$	$1/2\langle 110\rangle$	$1/3\langle 111\rangle$
10 keV	Ni	0.4–3.865	0.5–7.245		
	Ni–Co–Fe	Not found			
30 keV	Ni	5.4–104.343	7.7–111.547	1.3–9.653	0.2–6.265
	Ni–Co–Fe	1.7–19.502	4.0–45.090	0.7–4.908	0.1–1.668
50 keV	Ni	7.2–110.033	10.4–137.527	1.2–16.483	0.2–5.668
	Ni–Co–Fe	8.1–108.298	8.7–131.661	1.0–7.692	

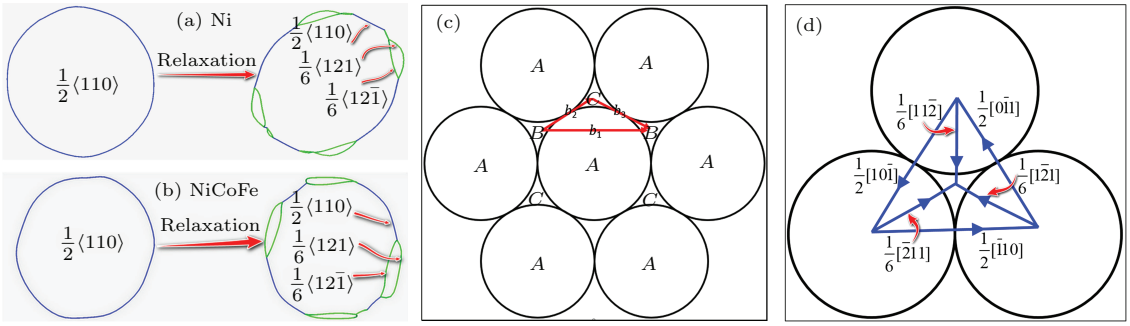


Fig. 8. The evolution of $1/2\langle 110\rangle$ dislocation loop in Ni (a) and NiCoFe MEAs (b). (c) Slip of $\{111\}$ planes in FCC metals. (d) Burger vectors of perfect and Shockley partial dislocations in the $\{111\}$ plane. The lines of different colors represent dislocations with different Burgers vectors, where green is a Shockley ($1/6\langle 112\rangle$), purple a stair-rod ($1/6\langle 110\rangle$), light blue a Frank ($1/3\langle 111\rangle$), yellow a Hirth ($1/3\langle 001\rangle$), and dark blue a perfect dislocation ($1/2\langle 110\rangle$).

Simultaneously, the formation process of the SFT structure was also studied (Fig. 9). First, a half atomic layer was extracted in the Ni and Ni–Co–Fe bulk to construct an intrinsic $1/3\langle 111\rangle$ dislocation loop (Figs. 9(a) and 9(c)). Then, the model was minimized by energy to attain equilibrium. In Ni, the $1/3\langle 111\rangle$ dislocation loop is dissociated and does not form a complete stacking fault tetrahedron (Fig. 9(b)). However, in NiCoFe MEAs, the $1/3\langle 111\rangle$ dislocation loop transforms into a complete stacking fault tetrahedron (Fig. 9(d)). The animated maps of the evolution process can be seen in supplementary movies 1–4.

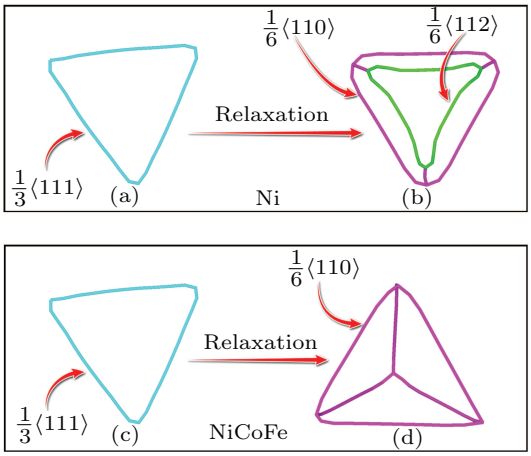


Fig. 9. Formation process of SFT structure in pure Ni and NiCoFe MEAs. The lines of different colors represent dislocations with different Burgers vectors, where green is a Shockley ($1/6\langle 112\rangle$), purple a stair-rod ($1/6\langle 110\rangle$), light blue a Frank ($1/3\langle 111\rangle$).

From supplementary movies 1–4, the evolution process can be summarized as shown in Fig. 10. First, a triangular Frank dislocation loop was constructed by extracting half of the atomic layer (Fig. 10(a)). The three sides of $\overrightarrow{AB}$, $\overrightarrow{BC}$, and $\overrightarrow{CA}$ are the Frank partial dislocations on the $b = \overrightarrow{\delta D}$ plane, and δ is a layer of fault. Each Frank's partial dislocation is dissociated on a close-packed plane containing the dislocation line, such as the $\overrightarrow{AB}$ dislocation is dissociated on the γ plane $\overrightarrow{\delta D} = \overrightarrow{\delta\gamma} + \overrightarrow{\gamma D}$. The Frank partial may dissociate into a low-energy stair-rod dislocation and a Shockley partial on an intersecting slip plane according to the reaction

$$\frac{1}{3}[111] \rightarrow \frac{1}{6}[101] + \frac{1}{6}[121]. \tag{2}$$

Detailed information on the decomposition can be seen in Fig. 10(b). In this way, the triangular Frank dislocation loop is dissociated into three stair-rods $\overrightarrow{AB}$, $\overrightarrow{BC}$, and $\overrightarrow{CA}$ with Burger vectors of $\overrightarrow{\delta\gamma}$, $\overrightarrow{\gamma\alpha}$, and $\overrightarrow{\delta\beta}$, respectively, and three Shockley partial dislocations $\overrightarrow{AB}$, $\overrightarrow{BC}$, and $\overrightarrow{CA}$ with Burgers vectors of $\overrightarrow{\gamma D}$, $\overrightarrow{\alpha D}$, and $\overrightarrow{\beta D}$, respectively. Figure 10(c) shows that because the Burgers' vectors of the stair-rod and Shockley partial dislocations intersect at an acute angle and repel each other, the Shockley partial dislocation moves upon its slip plane, and their two ends are pinned by the stair-rod, which bends into a bow (Fig. 9(b)). Two Shockley partial dislocations attract each other and slip; the arcuate area expands until the Shockley partial dislocation reacts to form a stair-rod dislocation

$$\frac{1}{6}[121] + \frac{1}{6}[\overline{2}11] \rightarrow \frac{1}{6}[\overline{1}10]. \tag{3}$$

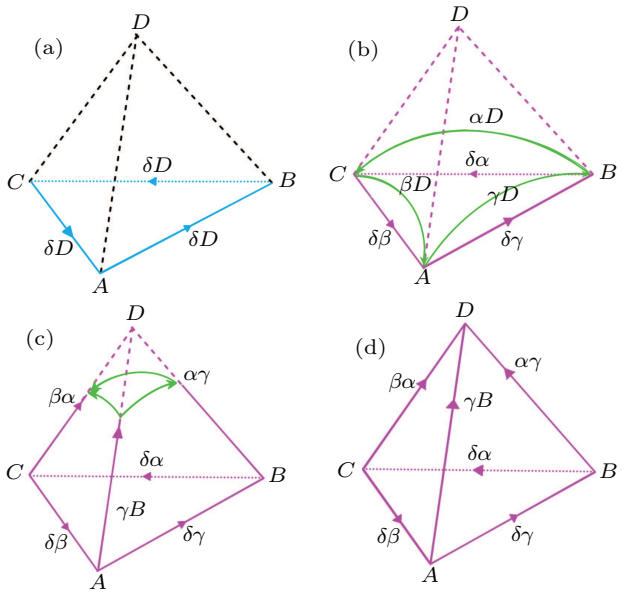


Fig. 10. The formation process of stacking fault tetrahedron in FCC crystal. The lines of different colors represent dislocations with different Burgers vectors, where green is a Shockley ($1/6\langle 112\rangle$), purple a stair-rod ($1/6\langle 110\rangle$), light blue a Frank ($1/3\langle 111\rangle$), the dot lines are for guiding the eyes.

Thus, eventually forming an SFT defect (Fig. 10(d)). Similar processes for forming SFT structures have also been observed in experiments and simulations before.[52–55] However, we can comply with the difference in the evolution process of $1/3\langle 111\rangle$ dislocation loops in Ni and NiCoFe MEAs (Figs. 9(b) and 9(d)). To determine possible reasons for this difference, the intrinsic stacking faults for FCC Ni and NiCoFe MEAs were constructed. The stacking fault energy (SFE) of Ni and Ni–Co–Fe alloys produced herein and DFT calculations[56,57] are listed in Table 4. The SFE of NiCoFe MEA is $\sim 26 \pm 12$ mJ/m^2, which is slightly lower than the results of the previous DFT studies,[31,57–59] while much lower than the value of Ni (112 mJ/m^2). A previous study[60] has shown that the SFE value of individual elements in the system is critical for that of the resultant alloy, either increasing the constituents having low SFE or reducing those with high SFE tends to lead to the HEA or MEA, which has lower SFE. However, the result of SFE in the NiCoFe MEAs is an average of 10 different random samples with different configurations, which is a statistically averaged result. The results show that the stacking fault energy of NiCoFe MEAs is much lower than that of pure Ni, indicating that the partial dislocations in the NiCoFe MEAs are easy to associate because of relatively narrow separations. Therefore, the Shockley partial dislocations in Ni do not completely form stair-rod dislocations, probably

due to the relatively high SFE in Ni, which limits the Shockley dislocation slip to form stair-rod dislocations. As the composition of the alloy increases, the SFE is reduced, which is consistent with the previous results,[59,60] so that the Shockley partial dislocation completely forms the stair-rod dislocations in the ternary NiCoFe MEAs.

Table 4. Comparison of stacking fault energy of Ni and NiCoFe MEAs with DFT calculations.

Alloy	SFE (mJ/m^2) Present work	SFE (mJ/m^2) DFT
Ni	112	121,[51] 110[52]
Ni–Co–Fe	26±12	56,[33] 56±35,[53] 67±12[54]

4. Conclusion

In summary, we have conducted MD simulations to investigate the formation and evolution of radiation defects in NiCoFe MEAs, and compared the results with that of pure Ni. Through a series of research and analyses, it is found that with the increasing chemical disorder from pure Ni to ternary NiCoFe MEAs, the chemical disorder can substantially reduce the speed of energy dissipation resulting in less deleterious defects. Unlike the 1D motion mode in pure Ni, the migration of the defect clusters in Ni–Co–Fe occurs in 3D motion, resulting in the concentrated distribution of defects caused by radiation in NiCoFe MEAs, which benefits the self-recombination of defects. Thus, the number of defects and defect clusters finally produced are smaller than that in pure Ni, suggesting higher radiation tolerance of NiCoFe MEAs.

Simultaneously, the formation and evolution of dislocation loops in NiCoFe MEAs and pure Ni have been considered. The main types of dislocation loops are Shockley dislocation (1/6⟨112⟩), stair-rod dislocation (1/6⟨110⟩), Frank dislocation (1/3⟨111⟩), and perfect dislocation (1/2⟨110⟩). Quantitatively, there are more dislocation loops generated in Ni after radiation. Also, the dislocation loop is mainly a relatively complex dislocation network, which is due to the number of dislocation reactions in the FCC structure. Further, the dislocation reaction of dislocation loops in NiCoFe MEAs and pure Ni have been studied. The perfect dislocation loop spontaneously dissociates into two Shockley dislocations (1/6⟨112⟩), and the SFE of pure Ni is higher than those in NiCoFe MEAs, which is the reason why the Frank partial dislocation forms a perfect SFT in NiCoFe MEAs, but not in Ni. These results reveal that our MD simulations are reliable and provide atomic-level knowledge for understanding the irradiation resistance of the NiCoFe MEAs.

Acknowledgements

This work was financially supported by the National Natural Science Foundation of China (Grant No. 11775074) and the Science and Technology Program of Hunan Province, China (Grant No. 2019TP1014). The authors also thank the National Supercomputer Center in Changsha for the computational resource provided.

References

[1] Davis J R 1990 *ASM Speciality Handbook: Nickel, Cobalt, and Their Alloys*, 2nd edn. (New York: ASM International)
[2] Granberg F, Nordlund K, Ullah M W, Jin K, Lu C, Bei H, Wang L M, Djurabekova F, Weber W J and Zhang Y 2016 *Phys. Rev. Lett.* **116** 135504
[3] Lu C, Niu L, Chen N, Jin K, Yang T, Xiu P, Zhang Y, Gao F, Bei H, Shi S, He M R, Robertson I M, Weber W J and Wang L 2016 *Nat. Commun.* **7** 13564
[4] Cantor B, Chang I T H, Knight P and Vincent A J B 2004 *Mater. Sci. Eng. A* **375** 213
[5] Otto F, Yang Y, Bei H and George E P 2013 *Acta Mater.* **61** 2628
[6] Senkov O N, Miller J D, Miracle D B and Woodward C 2015 *Nat. Commun.* **6** 6529
[7] Jin K and Bei H 2018 *Front. Mater.* **5** 26
[8] Gludovatz B, Hohenwarter A, Catoor D, Chang E H, George E P and Ritchie R O 2014 *Science* **345** 1153
[9] Miracle D B and Senkov O N 2017 *Acta Mater.* **122** 448
[10] Yeh J W, Chen S K, Lin S J, Gan J Y, Chin T S, Shun T T, Tsau C H and Chang S Y 2004 *Adv. Eng. Mater.* **6** 299
[11] Zhang Y, Yang X and Liaw P K 2012 *JOM* **64** 830
[12] Senkov O N, Scott J M, Senkova S V, Miracle D B and Woodward C F 2011 *J. Alloys Compd.* **509** 6043
[13] Antonaglia J, Xie X, Tang Z, Tsai C W, Qiao J W, Zhang Y, Laktionova M O, Tabachnikova E D, Yeh J W, Senkov O N, Gao M C, Uhl J T, Liaw P K and Dahmen K A 2014 *JOM* **66** 2002
[14] Chuang M H, Tsai M H, Wang W R, Lin S J and Yeh J W 2011 *Acta Mater.* **59** 6308
[15] Tang Z, Huang L, He W and Liaw P 2014 *Entropy* **16** 895
[16] Lee C P, Chen Y Y, Hsu C Y, Yeh J W and Shih H C 2008 *Thin Solid Films* **517** 1301
[17] Santodonato L J, Zhang Y, Feygenson M, Parish C M, Gao M C, Weber R J, Neuefeind J C, Tang Z and Liaw P K 2015 *Nat. Commun.* **6** 5964
[18] Li Z, Pradeep K G, Deng Y, Raabe D and Tasan C C 2016 *Nature* **534** 227
[19] Zhang Y, Stocks G M, Jin K, Lu C, Bei H, Sales B C, Wang L, Beland L K, Stoller R E, Samolyuk G D, Caro M, Caro A and Weber W J 2015 *Nat. Commun.* **6** 8736
[20] Lu C, Jin K, Beland L K, Zhang F, Yang T, Qiao L, Zhang Y, Bei H, Christen H M, Stoller R E and Wang L 2016 *Sci. Rep.* **6** 19994
[21] Jin K, Lu C, Wang L M, Qu J, Weber W J, Zhang Y and Bei H 2016 *Scr. Mater.* **119** 65
[22] Kumar N A P K, Li C, Leonard K J, Bei H and Zinkle S J 2016 *Acta Mater.* **113** 230
[23] Lu C, Yang T N, Jin K, Velisa G, Xiu P, Peng Q, Gao F, Zhang Y, Bei H, Weber W J and Wang L 2019 *J. Nucl. Mater.* **524** 60
[24] Lu C, Yang T, Jin K, Velisa G, Xiu P, Song M, Peng Q, Gao F, Zhang Y, Bei H, Weber W J and Wang L 2018 *Mater. Res. Lett.* **6** 584
[25] Lu C, Yang T, Jin K, Gao N, Xiu P, Zhang Y, Gao F, Bei H, Weber W J, Sun K, Dong Y and Wang L 2017 *Acta Mater.* **127** 98
[26] Aidhy D S, Lu C, Jin K, Bei H, Zhang Y, Wang L and Weber W J 2015 *Acta Mater.* **99** 69
[27] Jin K, Bei H and Zhang Y 2016 *J. Nucl. Mater.* **471** 193
[28] Shan C, Lang L, Yang T, Lin Y, Gao F, Deng H and Hu W 2020 *Comput. Mater. Sci.* **177** 109555
[29] Ardell A J and Bellon P 2016 *Curr. Opin. Solid State Mater. Sci.* **20** 115
[30] Plimpton S 1995 *J. Comput. Phys.* **117** 1
[31] Lee B J and Baskes M I 2000 *Phys. Rev. B* **62** 8564
[32] Choi W M, Jo Y H, Sohn S S, Lee S and Lee B J 2018 *npj Comput. Mater.* **4** 1
[33] Do H S and Lee B J 2018 *Sci. Rep.* **8** 16015
[34] Fang Q, Chen Y, Li J, Jiang C, Liu B, Liu Y and Liaw P K 2019 *Int. J. Plast.* **114** 161
[35] Biersack J P and Ziegler J F 1982 *Nucl. Instrum. Methods Phys. Res.* **194** 93
[36] Liu X, Pei Z and Eisenbach M 2019 *Mater. Des.* **180** 107955

[37] Stukowski A, Bulatov V V and Arsenlis A 2012 *Modell. Simul. Mater. Sci. Eng.* **20** 085007
[38] Stukowski A 2010 *Modell. Simul. Mater. Sci. Eng.* **18** 015012
[39] Sigle W and Seeger A 1994 *Phys. Status Solidi A* **146** 57
[40] Urban K and Yoshida N 2006 *Philos. Mag. A* **44** 1193
[41] Tsai K Y, Tsai M H and Yeh J W 2013 *Acta Mater.* **61** 4887
[42] Zhang R, Zhao S, Ding J, Chong Y, Jia T, Ophus C, Asta M, Ritchie R O and Minor A M 2020 *Nature* **581** 283
[43] Lang L, Deng H Q, Tian Z, Gao F, Hu W Y, Wen D D and Mo Y F 2019 *J. Alloys Compd.* **775** 1184
[44] Lu C, Yang T, Niu L, Peng Q, Jin K, Crespillo M L, Velisa G, Xue H, Zhang F, Xiu P, Zhang Y, Gao F, Bei H, Weber W J and Wang L 2018 *J. Nucl. Mater.* **509** 237
[45] Arakawa K, Ono K, Isshiki M, Mimura K, Uchikoshi M and Mori H 2007 *Science* **318** 956
[46] Matsukawa Y and Zinkle S J 2007 *Science* **318** 959
[47] Foreman A J E, Phythian W J and English C A 1992 *Philos. Mag. A* **66** 671
[48] Zhao P and Shimomura Y 1999 *Comput. Mater. Sci.* **14** 84
[49] Levo E, Granberg F, Fridlund C, Nordlund K and Djurabekova F 2017 *J. Nucl. Mater.* **490** 323
[50] Yi X, Jenkins M L, Kirk M A, Zhou Z and Roberts S G 2016 *Acta Mater.* **112** 105
[51] Zhang J Y and Zhang W Z 2019 *Modell. Simul. Mater. Sci. Eng.* **27** 035008
[52] Gao F and Bacon D J 1997 *Philos. Mag. A* **75** 1603
[53] Nordlund K and Gao F 1999 *Appl. Phys. Lett.* **74** 2720
[54] Diaz de la Rubia T and Guinan M W 1991 *Phys. Rev. Lett.* **66** 2766
[55] Béland L K, Lu C, Osetskiy Y N, Samolyuk G D, Caro A, Wang L and Stoller R E 2016 *J. Appl. Phys.* **119** 085901
[56] Carter C B and Holmes S M 2006 *Philos. Mag.* **35** 1161
[57] Siegel D J 2005 *Appl. Phys. Lett.* **87** 121901
[58] Zaddach A J, Niu C, Koch C C and Irving D L 2013 *JOM* **65** 1780
[59] Zhao S, Stocks G M and Zhang Y 2017 *Acta Mater.* **134** 334
[60] Liu S F, Wu Y, Wang H T, He J Y, Liu J B, Chen C X, Liu X J, Wang H and Lu Z P 2018 *Intermetallics* **93** 269